Title
Inferior Olivary TMEM16B Mediates Cerebellar Motor Learning

Journal
Neuron, 95(5)

ISSN
0896-6273

Authors
Zhang, Yang
Zhang, Zhushan
Xiao, Shaohua
et al.

Publication Date
2017-08-01

DOI
10.1016/j.neuron.2017.08.010

Peer reviewed

HHS Public Access

Author manuscript

Neuron. Author manuscript; available in PMC 2018 August 30.

Published in final edited form as:

Neuron. 2017 August 30; 95(5): 1103–1111.e4. doi:10.1016/j.neuron.2017.08.010.

Inferior olivary TMEM16B mediates cerebellar motor learning

Yang Zhang[1,†], **Zhushan Zhang**[1,†], **Shaohua Xiao**[3], **Jason Tien**[3], **Son Le**[1], **Trieu Le**[1], **Lily Y. Jan**[3,*], and **Huanghe Yang**[1,2,4,*]

[1]Department of Biochemistry, Duke University Medical Center, Durham, NC, 27710 USA

[2]Department of Neurobiology, Duke University Medical Center, Durham, NC, 27710 USA

[3]Departments of Physiology, Biochemistry and Biophysics, Howard Hughes Medical Institute, University of California, San Francisco, San Francisco, CA, 94158 USA

SUMMARY

Ca^{2+}-activated ion channels shape membrane excitability and Ca^{2+} dynamics in response to cytoplasmic Ca^{2+} elevation. Compared to the Ca^{2+}-activated K^+ channels known as BK and SK channels, the physiological importance of Ca^{2+}-activated Cl^- channels (CaCCs) in neurons has been largely overlooked. Here we report that CaCCs coexist with BK and SK channels in inferior olivary (IO) neurons that send climbing fibers to innervate cerebellar Purkinje cells for the control of motor learning and timing. Ca^{2+} influx through the dendritic high-threshold voltage-gated Ca^{2+} channels activates CaCCs, which contribute to membrane repolarization of IO neurons. Loss of TMEM16B expression resulted in the absence of CaCCs in IO neurons, leading to markedly diminished action potential firing of IO neurons in TMEM16B knockout mice. Moreover, these mutant mice exhibited severe cerebellar motor learning deficits. Our findings thus advance the understanding of the neurophysiology of CaCCs and the ionic basis of IO neuron excitability.

INTRODUCTION

The interplay between Ca^{2+}-permeable channels and Ca^{2+}-sensitive channels shapes the membrane excitability of many cell types (Fakler and Adelman, 2008; Hille, 2001). As major mediators for depolarization-induced Ca^{2+} entry in virtually every excitable cell type, voltage-gated Ca^{2+} (Ca_V) channels cause activation of Ca^{2+}-sensitive ion channels, which

*Correspondence should be addressed to H.Y. (huanghe.yang@duke.edu) and L.Y.J (lily.jan@ucsf.edu).
4Lead contact.
†These authors contributed equally to this work.

COMPETING FINANCIAL INTERESTS

The authors declare no competing financial interests.

SUPPLEMENTAL INFORMATION

Supplemental Information includes four figures can be found with this article online at

AUTHOR CONTRIBUTIONS

Conceptualization, L.Y.J. and H.Y.; Methodology, Y.Z. and Z.Z., Resources, J.T. and S.X.; Investigation, Y.Z., Z.Z., S.X., S.L. and T.L.; Formal analysis, Y.Z., Z.Z. and H.Y.; Software, Y.Z.; Writing – Original Draft, H.Y., Y.Z., Z.Z. and L.Y.J.; Writing – Review & Editing, H.Y.; Funding Acquisition, H.Y. and L.Y.J.; Supervision, H.Y. and L.Y.J.

modulate the manner in which Ca_V channels regulate action potential firing, muscle contraction, secretion and gene expression (Catterall, 2011; Hille, 2001). Ca^{2+}-activated K^+ (K_{Ca}) channels of large conductance, the BK channels, and K_{Ca} channels of small conductance, the SK channels, are the most extensively studied Ca^{2+}-sensitive ion channels that serve as Ca^{2+} sensors and feedback regulators of Ca_V channels (Fakler and Adelman, 2008; Sah and Faber, 2002; Salkoff et al., 2006; Stocker, 2004). Opening of these K_{Ca} channels elicits hyperpolarizing K^+ conductance, which in turn facilitates Ca_V channel deactivation. In many neurons, BK and SK channels are believed to contribute to the fast after-hyperpolarization (fAHP) and medium after-hyperpolarization (mAHP) of an action potential, respectively (Sah and Faber, 2002; Stocker, 2004). In addition, K_{Ca} channels, especially SK channels, can also contribute to pacemaking, spike frequency adaptation and synaptic integration (Bond et al., 2005; Sah and Faber, 2002).

Inferior olivary (IO) neurons in the brain stem have been extensively studied with respect to how functional coupling between Ca_V and K_{Ca} channels controls membrane excitability (Llinas and Yarom, 1981a, b) (Figures S1A, S1B and S1C). The interplay between Ca_V and BK/SK channels is proposed to define IO neuronal firing (Choi et al., 2010; Lang et al., 1997; Llinas and Yarom, 1981a, b), which is transmitted via the climbing fibers to trigger complex spikes of Purkinje cells in the cerebellum thereby regulating cerebellar motor learning and timing (De Gruijl, 2013; De Zeeuw et al., 1998; Llinas, 2013). Generation of a fast somatic Na^+ spike of an IO neuron via current injection is followed by a prominent after-depolarization (ADP) mediated by the dendritic high-threshold Ca_V channels (Figure S1D). It has been proposed that the high-threshold Ca_V channels in IO neurons activate dendritic K_{Ca} channels, which mediate fast membrane repolarization and prolonged AHP (Choi et al., 2010; Lang et al., 1997; Llinas and Yarom, 1981a, b). However, electrophysiological and pharmacological characterizations suggest that BK channels are primarily expressed in the soma (Lang et al., 1997), where they presumably form complexes with T-type Ca_V channels to regulate the generation of spontaneous subthreshold oscillation (SSTO) and low threshold spikes (LTS) of IO neurons. Consequently, SK channels have been considered as the major K_{Ca} channels in the dendrites to respond to the high-threshold Ca_V channel-induced Ca^{2+} entry (Bal and McCormick, 1997; Lang et al., 1997) (Figure S1A). As SK and Ca_V channels are usually localized within microdomains (~20–200 nm apart) (Fakler and Adelman, 2008), SK channels are believed to mainly contribute to mAHP due to the time delay required for Ca^{2+} diffusion from Ca_V channels to SK channels (Stocker, 2004). It is unclear, however, which Ca^{2+}-activated ion channels contribute to repolarization in the IO dendrites to terminate the ADP.

In this study, we characterized the Ca^{2+}-sensitive conductance in IO neurons and discovered an unexpected, additional Ca^{2+}-activated conductance distinct from those mediated by BK and SK K_{Ca} channels. We found that the recently identified TMEM16B Ca^{2+}-activated Cl^- channel (CaCC) is responsible for this newly identified IO conductance. TMEM16B-CaCC is activated by Ca^{2+} influx through the dendritic high-threshold Ca_V channels and serves as the major repolarizing current that negatively regulates these Ca_V channels and rapidly terminates the ADP. Genetic deletion or pharmacological inhibition of TMEM16B-CaCC channels prolonged the durations of both ADP and AHP, resulting in prominent reduction of IO neuron firing. Consistent with our findings from brain stem slice recordings, TMEM16B

deficient mice exhibit markedly reduced motor learning capability as revealed by the eyeblink classical conditioning assay. Our study thus identifies TMEM16B-CaCC as a newly identified Ca^{2+}-sensitive conductance in IO neurons and ascribes this Ca^{2+}-activated Cl^- channel physiological functions important in controlling IO neuron firing and cerebellar motor learning.

RESULTS

Ca^{2+}-activated chloride current (CaCC) in the inferior olivary (IO) neurons

We first conducted whole cell voltage clamp measurement of IO neurons in acutely isolated brain stem slices (Figure 1A). In the presence of 5 mM QX314, 110 mM Cs^+ and 20 mM tetraethylammonium (TEA), voltage-gated Na^+ (Na_V) channels and the majority of K^+ channels including BK and SK channels were blocked. According to the established ionic current model of the IO neurons (Bal and McCormick, 1997; Lang et al., 1997; Llinas and Yarom, 1981a, b) (Figure S1A), high-threshold Ca_V channels should account for the major ion conductance under this experimental condition. Unexpectedly, instead of observing a slow-inactivating, inward Ca^{2+} current upon depolarization to +10 mV, we recorded an initial transient inward current (Figure 1A, inset), followed by a large, time-dependent outward current (I_{tdo}) during membrane depolarization, and a slowly deactivating tail current (I_{tail}) that lasted for more than one second when the membrane potential was returned to −80 mV (Figure 1A).

To investigate the ionic basis underlying this unexpected conductance, we applied 400 μM extracellular Cd^{2+}, a potent Ca_V channel blocker (Catterall et al., 2005), to IO neurons (Figure 1A). We found that Cd^{2+} not only abolished the transient inward current, it also eliminated the I_{tdo} and I_{tail}. This suggested that this newly identified conductance is likely activated by the Ca_V channel-mediated Ca^{2+} influx; the inward current through Ca_V channels appeared to be rapidly overridden by the large outward I_{tdo} current, resulting in the initial transient inward current. With Ca_V channels blocked by Cd^{2+}, membrane depolarization alone was insufficient to open the channel that conducts the outward I_{tdo} current, so this channel is likely a Ca^{2+}-activated ion channel. For further validation, we tested whether the newly identified conductance is sensitive to the duration of the high-threshold Ca_V channel opening that would determine the extent of Ca^{2+} entry. Indeed, we found that the peak amplitudes of I_{tdo} and I_{tail} were increased and the kinetics of I_{tail} significantly slowed by prolonging the depolarization for high-threshold Ca_V channel activation (Figures S1E, S1F and S1G). This finding further supports the notion that this newly identified conductance arises from a Ca^{2+}-activated ion channel.

This Ca^{2+}-activated ion channel is insensitive to blockers of BK and SK K_{Ca} channels such as Cs^+ and TEA, but it can be largely blocked by 100 μM niflumic acid (NFA), a widely used Cl^- channel blocker (Figures 1A and 1B). Based on its Ca^{2+} sensitivity and pharmacological profiles, as well as its slow activation and deactivation kinetics, we hypothesized that the newly identified Ca^{2+}-activated channel in IO neurons is likely to be a canonical CaCC (Hartzell et al., 2005; Pedemonte and Galietta, 2014). To test this hypothesis, we decreased the extracellular Cl^- concentration from 136.8 mM (E_{Cl} = −40.4 mV) to 28 mM (E_{Cl} = 0 mV) to see whether the reversal potential is sensitive to this

alteration of Cl^- concentration (Figures 1C and 1D). Indeed, the reversal potential was shifted by ~30 mV when switching to the low extracellular Cl^- solution, indicating that this Ca^{2+} activated conductance was mediated by a Cl^- channel. The small deviation from the theoretical prediction of 40 mV shift could have arisen from the presence of a residual high-threshold Ca^{2+} current at 0 mV, a finite albeit small cation permeability of the CaCC channels (Pifferi et al., 2009), and space clamp inaccuracy due to the electrical coupling of IO neurons (De Gruijl, 2013). In summary, we discovered a previously unreported Ca^{2+}-activated Cl^- channel that is highly expressed in IO neurons.

TMEM16B but not TMEM16A encodes the CaCC in IO neurons

TMEM16A and TMEM16B are two recently discovered CaCCs with canonical CaCC characteristics (Caputo et al., 2008; Schroeder et al., 2008; Yang et al., 2008). According to Allen Brain Atlas, transcripts of TMEM16B, but not TMEM16A, are highly expressed in the IO (Figures S2A and S2B). Consistent with the *in situ* hybridization data, our immunofluorescence results showed that TMEM16B protein, but not TMEM16A protein, is highly expressed in IO neurons (Figures 2A and 2B).

In order to further verify TMEM16B expression and to study the physiological function of the CaCC in the IO neurons, we generated TMEM16B knockout (KO) mice by inserting the coding sequence for farnesylated mCherry (mCherry-F) in-frame at the alternative start site in Exon3 of *Tmem16B* (Figure S2C). The disruption of Exon3 led to greatly reduced expression of TMEM16B mRNA in the IO nucleus, as well as the retina, olfactory bulb and hippocampus (Figures S2D and S2E), regions that have previously been reported to express TMEM16B (Billig et al., 2011; Huang et al., 2012b; Stohr et al., 2009). TMEM16B KO mice displayed no detectable TMEM16B protein expression in the IO nucleus (Figures 2C and S2E), while membrane-associated mCherry-F expression in the IO nucleus revealed the presence of neurons that normally express TMEM16B (Figure S2F). There was no upregulation of TMEM16A protein in the TMEM16B deficient IO neurons (Figure S2G). So it seemed likely that the IO CaCC would be completely eliminated in TMEM16B KO mice. Indeed, the time-dependent I_{tdo} and I_{tail} were absent in IO neurons of TMEM16B KO mice (Figure 2D, 2E and 2F). These experiments demonstrate that TMEM16B-CaCC accounts for the newly identified Ca^{2+}-activated conductance in IO neurons.

The dendritic high-threshold Ca_V channels fuel TMEM16B-CaCC

Next, we characterized IO neurons with or without TMEM16B by varying membrane potential. In TMEM16B deficient IO neurons, membrane depolarization from −20 to +40 mV elicited a rapidly activating inward current that resembles the current conducted by high threshold Ca_V channels (Figures 3A and 3C). In contrast, WT IO neurons exhibited a prominent slow-activating outward current that is mediated by Cl^- influx through TMEM16B CaCC, when the membrane potential was depolarized beyond −10 mV (Figures 3B and 3C). The appearance of the CaCC current following Ca_V channel opening indicates that TMEM16B-CaCC activation is triggered by Ca^{2+} influx through the dendritic high-threshold Ca_V channels. As the IO ADP would typically bring the membrane potential to around −10 to 0 mV (Figure S1D), the Cl^- influx through the TMEM16B-CaCC during

ADP will cause hyperpolarization and provide a negative feedback to the high-threshold Ca_V channels, so as to accelerate the deactivation of Ca_V channels and the ADP termination.

To further study the coupling between TMEM16B-CaCC and high-threshold Ca_V channels, we increased the EGTA concentration in the solution within the patch clamp electrode from 0.2 mM to 5 mM. Right after break-in with the patch clamp electrode, when the cytosolic content was still largely intact, a 50 ms pulse of depolarization to 0 mV elicited a transient inward current and an outward CaCC current, followed by a large, slowly deactivating CaCC tail current at the end of the depolarization pulse (Figure 3D). After EGTA dialyzed into the IO neuron through the patch pipette, both the outward CaCC peak current and the CaCC tail current gradually diminished over time (Figure 3E). After 4 minutes of whole-cell patch recording, the outward CaCC peak current and the slow CaCC tail current were completely eliminated. As EGTA is a slow acting Ca^{2+} chelator with slow on-rate for Ca^{2+} binding (Neher, 1998), the capability of EGTA to completely abolish the TMEM16B-CaCC current suggested that TMEM16B-CaCC likely resides in the microdomain of high-threshold Ca_V channels where the Ca^{2+} ions entering the neuron through Ca_V channels need to travel tens of nanometers before acting on the CaCCs. When we gradually prolonged the 0 mV depolarization from 100 to 400 ms so as to introduce more Ca^{2+} into the cell, Ca^{2+} ions within the microdomain accumulated and eventually reached a level beyond the buffering capacity of EGTA, leading to the re-appearance of the outward CaCC peak current and slow deactivating CaCC tail current (Figure 3F). Based on these observations, we conclude that TMEM16B-CaCC is highly expressed within the microdomains of the dendritic high-threshold Ca_V channels so that it can be activated due to the Ca^{2+} influx through the high-threshold Ca_V channels. The opening of TMEM16B-CaCC in turn triggers the hyperpolarization to shut down the Ca_V channels. Therefore, TMEM16B-CaCC is responsible for the repolarizing conductance in the IO dendrites.

TMEM16B-CaCC participates in membrane repolarization to terminate ADP and regulate IO neuron firing

To understand how the dynamic interplay between the TMEM16B-CaCC and the high-threshold Ca_V channels might impact IO neuronal excitability, we examined the depolarization-induced firing of IO neurons in TMEM16B WT and KO mice. In response to a 1 second injection of 400 pA depolarizing current, TMEM16B deficient IO neurons exhibited marked reduction of firing compared to the WT IO neurons (Figures 4A, 4B and 4C). Not only did genetic removal of TMEM16B impair excitability, application of 100 μM NFA to WT IO neurons also greatly suppressed neuronal firing (Figure S3), suggesting that the TMEM16B-CaCC channel activity is important for IO neuronal excitability.

TMEM16B deficient IO neurons also exhibited significantly prolonged ADP and AHP (Figures 4D and 4E) and a much shallower slope for the decay of AHP (Figure 4F), which determines the readiness to fire the next action potential. As the dendritic high-threshold Ca_V channels are responsible for ADP generation (Llinas and Yarom, 1981a), the prolonged duration of ADP in TMEM16B deficient IO neurons suggests that TMEM16B-CaCC indeed serves as a major repolarizing conductance. This is consistent with the coupling between TMEM16B-CaCC and dendritic high-threshold Ca_V channels that is detectable under

voltage clamp (Figure 3). Loss of this repolarizing CaCC current in TMEM16B deficient IO neurons allows dendritic high-threshold Ca_V channels to open for a longer duration, during which more Ca^{2+} ions enter the dendrites. Moreover, longer time may be needed for Ca^{2+} clearing machinery including Ca^{2+} pumps, Ca^{2+} buffering and Ca^{2+} diffusion to remove excessive Ca^{2+} ions (Hille, 2001). During the prolonged Ca^{2+} elevation in IO dendrites, the dendritic Ca^{2+}-activated and voltage-insensitive SK channels can remain open for a longer period of time, resulting in prolonged AHP duration and slower recovery of the membrane potential from the AHP phase to fire the next action potential. Eventually excessive activation of SK channels downstream of dendritic Ca_V channels would cause IO neurons to cease firing. Our experiments demonstrate that TMEM16B-CaCC contributes to the repolarization of ADP and plays an important role in controlling IO neuron excitability.

TMEM16B is specifically expressed in IO neurons within the olivo-cerebellar system

Before characterizing the motor behavior of TMEM16B KO mice, we tested whether TMEM16B is also expressed in other types of neurons within the olivo-cerebellar system. The TMEM16B deficient mice that we generated are engineered to express mCherry-F in TMEM16B expressing cells (Figures S2C and S2F). In the cerebellar cortex and the deep cerebellar nucleus (DCN) of the TMEM16B KO mice, we only observed the mCherry signal from the climbing fibers (CF), the axons of IO neurons that innervate the Purkinje cells (PCs, Figure 5A) and the DCN neurons (Figure 5C). No other cell type in the cerebellum is mCherry positive (Figures 5A, 5B and 5C), indicating that TMEM16B expression is restricted to the IO nucleus within the olivo-cerebellar system (Figures S2B, 2B and S2F). Thus, any mutant phenotype involving motor behavior that depends on cerebellar activity must result from the alteration of the IO neuron excitability in TMEM16B KO mice.

TMEM16B deficient mice exhibit impaired motor learning

In the olivo-cerebellar system, the IO nucleus plays an essential role in controlling motor learning by sending strong climbing fiber inputs to Purkinje cells to modulate parallel fiber synaptic plasticity (De Gruijl, 2013; Llinas, 2013) (Figure S4A). In order to examine the physiological function of the TMEM16B-CaCC in IO neurons, we subjected WT and TMEM16B KO mice to eyeblink classical conditioning (Heiney et al., 2014), a well-established cerebellar learning behavioral test. A 2.7 Hz tone and a white light LED were co-applied as the conditioned stimuli (CS). Then a 100 ms air puff was given to the animals' eyes as the unconditioned stimulus (US) 250 ms after the initiation of the CS; the CS and US were terminated at the same time, 350 ms after the initiation of the CS. Eyelid deflection was continuously monitored with a high-speed monochrome camera under infrared illumination (Figure S4B), and the conditioned responses (CR) and unconditioned responses (UR) were quantified. This paired presentation of CS and US during training sessions gradually led to the development of CRs (Figure 6A). Whereas TMEM16B KO mice and WT controls had similar UR in response to the air puff, TMEM16B KO mice exhibited a significant delay in CR acquisition during the 7-day paired training sessions, as compared to WT mice (Figures 6B, S4C and S4D). WT mice started to respond to the CS at the end of the training section in Day 1. In contrast, TMEM16B KO mice only began to display CR on Day 3. While TMEM16B KO mice showed improvement over time, their CR acquisition was significantly smaller than that of WT mice (Figure 6B). It thus appears that the

markedly diminished IO neuron excitability led to severe cerebellar motor learning deficits of TMEM16B KO mice. Taken together, our study reveals that the TMEM16B-CaCC in IO neurons plays a critical role in controlling cerebellar motor learning.

DISCUSSION

Our discovery of a previously unknown Ca^{2+}-activated ion conductance in IO neurons has enabled us to elucidate its role in regulating IO neuronal excitability and cerebellar motor learning. We showed that TMEM16B-CaCC accounts for this newly identified Ca^{2+}-activated conductance in IO neurons. Thus, in addition to Ca^{2+}-activated BK and SK channels (Llinas and Yarom, 1981a, b; Sailer et al., 2004), IO neurons express Ca^{2+}-activated Cl^- channels (CaCCs). These Ca^{2+}-activated K^+ channels and Cl^- channels activate in response to intracellular Ca^{2+} elevation and collectively work on shaping the IO action potential waveform and firing pattern.

Compared to BK and SK channel, the contributions of CaCCs to the excitability of central neurons have received much less attention (Frings et al., 2000). TMEM16A corresponds to CaCCs (Caputo et al., 2008; Schroeder et al., 2008; Yang et al., 2008) in exocrine glands (Huang et al., 2009; Huang et al., 2012a; Scudieri et al., 2012; Yang et al., 2008), smooth muscle cells (Davis et al., 2010; Huang et al., 2009), interstitial cells of Cajal (ICC) (Chen et al., 2007; Gomez-Pinilla et al., 2009; Huang et al., 2009), and nociceptive dorsal root ganglion (DRG) neurons (Cho et al., 2012; Liu et al., 2010), where they facilitate Cl^- and fluid secretion, muscle contraction, pacemaking of gut contractility, and pain sensation, respectively. TMEM16B expression is mainly restricted to the nervous system including the hippocampus (Huang et al., 2012b) and olfactory bulb (Billig et al., 2011), and in sensory neurons (Pedemonte and Galietta, 2014). TMEM16B-CaCC is highly expressed in the photoreceptor terminals of mouse retina, where it may regulate the release of glutamate at the terminal via local feedback control of the activity of Ca_V channels (Mercer et al., 2011; Stohr et al., 2009). TMEM16B-CaCC is also abundantly expressed in the mouse nasal olfactory epithelium and vomeronasal sensory neurons, where it might be activated downstream of cyclic nucleotide-gated (CNG) channels and TRPC2 channels, respectively (Billig et al., 2011; Yang and Delay, 2010).

Here we discover that TMEM16B-CaCC in IO neurons plays an important role in mediating cerebellar motor learning as assessed via eyeblink classical conditioning. Having found a large CaCC current, we report that TMEM16B is highly expressed in IO neurons and is functionally coupled to the dendritic high-threshold Ca_V channels, the opening of which generates the long ADP in IO neurons. Based on the sensitivity of the Ca_V-CaCC coupling to the EGTA concentration, we predict that TMEM16B is located within microdomains of the high-threshold Ca_V channels in the IO dendrites; TMEM16B-CaCC is likely located 20–200 nm from these dendritic Ca_V channels. As TMEM16B-CaCC activation depends on both Ca^{2+} and voltage under physiological conditions (Pedemonte and Galietta, 2014), the open probability of TMEM16B-CaCC might sharply increase at the late phase of ADP when more Ca^{2+} ions from the high-threshold Ca_V channels reach the CaCC channels while the membrane potential remains depolarized. The large hyperpolarizing Cl^- current through TMEM16B can rapidly repolarize the membrane and shut down the high-threshold Ca_V

channels. Through this negative feedback mechanism, TMEM16B CaCC activity would limit the extent of Ca^{2+} influx and maintain the proper shape and duration of ADP essential for the normal firing pattern of IO neurons. Removal of this major repolarizing current genetically or pharmacologically results in prolonged ADP duration, more Ca^{2+} entry and longer AHP duration, thereby diminishing IO neuronal firing. Because only IO neurons express TMEM16B within the olivo-cerebellar system, loss of this effector of dendritic Ca_V channels in IO neurons is likely the major cause of impaired cerebellar motor learning in TMEM16B KO mice.

The correlation between reduced IO excitability and impaired cerebellar motor learning in TMEM16B KO mice adds new evidence to support the theory that IO excitability and the subsequent climbing fiber impulses play a key role on the formation of cerebellar motor learning (Lang et al., 2017; Najafi and Medina, 2013). The prevailing view of cerebellar motor learning is that IO neurons relay movement error signals through climbing fiber spikes to cause synaptic modification in the cerebellar cortex, such as long-term depression (LTD) of parallel fiber to Purkinje cell synapses (Lang et al., 2017). Recent studies have clearly shown that, during motor learning, the number of climbing fiber spikes and the duration of the bursts, which reflect IO excitable state, control the number of spikelets within a complex spike waveform and the duration of the complex spike responses in Purkinje cells (Coesmans et al., 2004; Mathy et al., 2009; Rasmussen et al., 2013; Yang and Lisberger, 2014). It is likely that the IO neurons from TMEM16B KO mice elicit fewer climbing fiber spikes, i.e., smaller burst size during eyeblink conditioning, which leads to shorter-duration complex spike responses in Purkinje cells, less calcium entry into Purkinje cell dendrites, smaller synaptic depression and thus weaker motor learning. Future *in vivo* characterization of TMEM16B KO mice will help to test this hypothesis.

It will be important to understand how three different Ca^{2+}-activated ion channels, namely CaCC, BK, SK channels, and two different Ca_V channels, which have high or low threshold for activation, orchestrate to control the membrane excitability of IO neurons. Taken together with previous findings, our study reveals that TMEM16B-CaCC, BK and SK channels not only have different biophysical properties (Adelman et al., 2012; Hartzell et al., 2005; Pedemonte and Galietta, 2014; Salkoff et al., 2006) but also are likely to have distinct subcellular distributions (Schweighofer et al., 1999). BK channel activation depends on both voltage and Ca^{2+}. Notwithstanding the dependence of Ca^{2+} sensitivity on BK channel composition, placement of BK channels in the vicinity of various Ca_V channels makes it possible for the high local Ca^{2+} concentration within nanodomains of Ca_V channels to activate BK channels (Berkefeld et al., 2006). Large single channel conductance and fast activation kinetics allow BK channels to rapidly hyperpolarize the membrane, thereby playing a major role in action potential repolarization and fast AHP (Lancaster and Nicoll, 1987; Storm, 1987). SK channels are usually located within microdomains of Ca_V channels (Fakler and Adelman, 2008). SK channels mainly contribute to the medium AHP phase, because of the longer distance between SK and Ca_V channels, and the high Ca^{2+} sensitivity and voltage-independence of SK channels. TMEM16B-CaCC channel properties differ from those of BK and SK channels in ways that may allow these Ca^{2+}-activated Cl^- channels to fulfill a range of physiological functions. First, its Ca^{2+} sensitivity is similar to that of SK channels but higher than that of BK channels (Adelman et al., 2012; Pedemonte and

Galietta, 2014; Salkoff et al., 2006). Second, unlike the voltage-dependent BK channels and the voltage-independent SK channels, TMEM16-CaCC channels have a hallmark activation profile: at submicromolar Ca^{2+} concentrations CaCC displays voltage dependent outward rectification, but it gradually loses voltage dependence when Ca^{2+} level is raised beyond a few micromolar (Pedemonte and Galietta, 2014). Third, TMEM16-CaCC currents have slow activation and deactivation kinetics under physiological conditions (Pedemonte and Galietta, 2014). Fourth, whereas K^+ current is always hyperpolarizing, the driving force for CaCC varies with the cell type and the physiological conditions (Frings et al., 2000). Depending on the cell type, developmental stages, subcellular compartments, and even different phases of an action potential, the CaCC-mediated Cl^- flux could be either hyperpolarizing or depolarizing (Frings et al., 2000). All these intriguing properties of TMEM16-CaCC endow it with the capability to play diverse roles in shaping membrane excitability. In the case of IO neurons, we found that TMEM16B-CaCC is mainly coupled to the dendritic high-threshold Ca_V channels when IO neurons receive strong excitatory inputs. It will be of interest to test in future studies whether TMEM16B-CaCC contributes to other aspects of IO neuronal physiology such as subthreshold membrane oscillations of IO neurons and olivo-cerebellar rhythmicity by coupling to different Ca^{2+} sources.

As one of the earliest physiological models established more than thirty years ago (Llinas and Yarom, 1981a, b), IO neurons have been extensively studied to improve our understanding of the physiological significance of the interplay between Ca_V channels and Ca^{2+}-activated K^+ channels. Our discovery of TMEM16B-CaCC in IO neurons and its ability to modulate dendritic Ca_V channel-mediated ADP and IO neuronal firing renders this physiological model system suitable for broader investigations of the cellular mechanisms and physiological impacts of Ca_V channels and Ca^{2+}-activated ion channels, which will not only help understand the role of the olivocerebellar system in motor learning and motor control, but shine lights on the mechanism of other neuronal processes.

STAR METHODS

KEY RESOURCES TABLE

REAGENT or RESOURCE	SOURCE	IDENTIFIER
Antibodies		
Mouse monoclonal anti-NeuN	EMD Millipore	Cat# MAB377; RRID:AB_2298772
Rabbit polyclonal anti-mCherry	Rockland	Cat# 600-401-P16S; RRID: AB_2614471
Mouse monoclonal anti-calbindin	Sigma Aldrich	Cat# C9848; RRID: AB_476894
Rabbit polyclonal anti- KCa1.1	Alomone labs	Cat# APC-021; RRID: AB_2313725
Rabbit polyclonal anti-KCa2.3	Alomone labs	Cat# APC-025; RRID:AB_2040130
Rabbit polyclonal anti-TMEM16A	Abcam	Cat# ab53212; RRID: AB_883075
Rabbit polyclonal anti-TMEM16B	(Huang et al., 2012)	N/A
Goat anti-Rabbit IgG (H+L), DyLight 488	Thermo Fisher Scientific	Cat# 35552; RRID: AB_844398
Goat anti-Rabbit IgG (H+L), Alexa Fluor 647	Thermo Fisher Scientific	Cat# A-21244; RRID:AB_2535812

REAGENT or RESOURCE	SOURCE	IDENTIFIER
Goat anti-mouse IgG (H+L), DyLight 488	Thermo Fisher Scientific	Cat# 35503; RRID: AB_1965946
Goat anti-mouse IgG (H+L), Alexa Fluor 647	Thermo Fisher Scientific	Cat# A-21235; RRID:AB_141693
Experimental Models: Mouse lines		
Mouse: TMEM16B knockout	This paper	N/A
Chemicals (Pharmacological compounds)		
QX-314	EMD MILLIPORE	Cat# 552233; CAS: CAS 21306- 56-9
Adenosine 5′-triphosphate magnesium salt	Sigma-Aldrich	Cat# A9187; CAS:74804-12-9
Cadmium chloride	Sigma-Aldrich	Cat# 202908; CAS:10108-64-2
Niflumic acid	Sigma-Aldrich	Cat# N0630; CAS: 4394-00-7
Sequence-Based Reagents		
Primer: atcataccgcggcatgtctccagaccttgaaagcc (identifying correctly targeted clones)	This paper	N/A
Primer: catctgtttgacaatccagccac (identifying correctly targeted clones)	This paper	N/A
Primer: ccatctactggataggcggg (genotyping)	This paper	N/A
Primer: tccatgtgcaccttgaagcg (genotyping)	This paper	N/A
Primer: attcatctcgctgctccctc (genotyping)	This paper	N/A
Software and Algorithms		
MATLAB (R2016b)	MathWorks	RRID:SCR_001622
Labview	National Instruments	RRID:SCR_014325
pClamp 10	Molecular Devices	RRID:SCR_011323
Origin 7.5	OriginLab Corp.	RRID:SCR_014212
Prism 7.0	GraphPad Software	RRID:SCR_002798
Adobe Illustrator CS6	Adobe	RRID:SCR_014198

CONTACT FOR REAGENT AND RESOURCE SHARING

Further information and requests for resources and reagents should be directed to and will be fulfilled by the Lead Contact, Huanghe Yang (huanghe.yang@duke.edu).

EXPERIMENTAL MODELS AND SUBJECT DETAILS

Both male and female mice were used for all experiments, and mice were randomly allocated to experimental groups. Adult mice aged 8–12 weeks were used for eyeblink classical conditioning experiments. Mice aged 10–16 days were used for brain slice recording. All mice were healthy with no obvious behavioral phenotype, and none of the experimental mice were immune compromised. Experimental mice were never involved in previous procedures or studies. Mice handling and use were carried out in a strict compliance with protocols approved by the Institutional Animal Care and Use Committee of Duke University, in accordance with National Institute of Health guideline. Mice were group housed and maintained on a regular 12-h light/dark cycle and all experiments were performed during the light phase. Food and water was provided ad libitum.

METHOD DETAILS

Generation of TMEM16B Knockout Mice—To generate the *TMEM16B* knockout mouse line, a 9.5kb genomic region flanking exon 3 of the *TMEM16B (or ANO2)* locus corresponding to chr6:125658999-125668464 of the mouse genome in the Ensembl Genome Browser was introduced into the PL253 retrieval vector as described (Liu et al., 2003). mCherry (Clonetech) with a farnesylation signal at the C-terminus (mCherry-F) was inserted in frame at the alternative start *ATG* in exon 3 of *TMEM16B*. A *NEO* cassette, which was driven by a PGK promoter and terminated with a BGH polyadenylation signal, was flanked by two FRT sites and engineered downstream of mCherry-F. The targeting vector was injected into 129/B6 F1 embryonic stem (ES) cells. Correctly targeted clones were identified by long-range PCR with primers (5′-ATCATACCGCGGCATGTCTCCAGACCTTGAAAGCC and 5′-CATCTGTTTGACAATCCAGCCAC). Microinjection of correctly targeted ES clones into C57BL/6 blastocysts was performed in the Gladstone Gene Transfer Core. Germline transmission from a chimeric male and subsequent genotyping were confirmed by PCR with primers (5′-CCATCTACTGGATAGGCGGG, 5′-TCCATGTGCACCTTGAAGCG, and 5′-ATTCATCTCGCTGCTCCCTC). The heterozygous (het) mice were backcrossed at least 10 generations into C57BL6 strain (N10). The het x het crosses resulted in offspring, which included knockout mice that were viable and fertile without noticeable differences compared to wild-type mice. PCR genotyping was performed on tail DNA extracted from such offspring.

Eyeblink Classical Conditioning—Delayed eyeblink classical conditioning was performed on a custom-made head-fixed eyeblink conditioning apparatus based on the design by Heiney and colleagues (Heiney et al., 2014). Briefly, experimental mice were surgically installed with a metal head plate to the skull using dental acrylic (Jet repair, Lang Dental) prior to behavioral tests. During experiments, animals were head-fixed to a metal rod and were free to walk on top of a foam cylinder at will. A high-speed camera and infrared LED illumination were mounted on a separate post via knuckle joints and were positioned at the side of the mouse's face. Two clamps in another post were used to hold a 23 gauge blunt needle for the air-puff unconditioned stimulus (US, ~ 4 psi pressure) and a breadboard holding a white LED for the light conditioned stimulus (CS) and a magnetic buzzer (5V, 2.7Hz) for the tone CS, respectively (Digi-key Electronics). A solenoid valve (Lee Products LTD) was connected to a low pressure air regulator to control the air puff. The entire apparatus was installed inside a Startle Sound Attenuating Cubicle (Med Associates) to isolate the animal from noise and ambient light. Custom-written software in Labview (National Instruments) was used to control a data acquisition system (National Instruments) to trigger US, CS and image acquisition of eyelid movements.

A total of 9 TMEM16B KO mice and 9 WT control mice (8–12 weeks) of either sex (6 males and 3 females for both genotypes) were used for the eyeblink conditioning experiments. A 2.7 Hz tone and a white light LED were co-applied for 350 ms as the CS, and a 100 ms air puff was applied 250 ms after the initiation of the CS as the US. The US and CS were co-terminated. Eyelid deflection was monitored with a high-speed monochrome camera under infrared illumination (Allied Vision). Each training session

consisted of 90 paired CS-US trials followed by 10 CS trials alone. Each mouse was trained for one session per day for seven consecutive days. The minimum interval between two trials was 15 s. Trials were only performed when the mouse eyelid was completely open. During training, mice were head-fixed but could walk freely on a foam cylinder. Eyelid movements were monitored from the video frames in each trial. Custom-written software was used to analyze the movement of eyelids in Matlab (Mathworks). Successful conditioned responses (CR) were defined by eyelid closure amplitudes of more than 15% of full closure. The successful CRs were calculated to assess the performance of the mice in each session. A repeated measure ANOVA was used for comparison of TMEM16B KO and WT mice in the same training session. Differences were set to be significant if $p < 0.05$ and highly significant if $p < 0.001$.

Immunostaining and Imaging—Mice were deeply anaesthetized using isoflurane, then perfused with phosphate buffered solution (PBS) followed with 4% paraformaldehyde (PFA) fixative through cardiac puncture. Brains were isolated and incubated in 4% PFA at 4°C overnight, followed by cryoprotection in 30% sucrose solution for 24 hours. 16 μm cerebellar-brain stem sections were cut sagittally using a cryostat (Leica). Sections were washed 10 minutes with PBS three times and incubated with 5% goat serum and 0.3% Triton X-100 for 2 hours at room temperature. Anti-mCherry rabbit antibody (Rockland, #600-401-P16S 1:800) was used to label mCherry-positive cells. Anti-calbindin monoclonal mouse antibody (Sigma Aldrich, #C9848, 1:1000) was used to label Purkinje cells of the cerebellum. Anti-NeuN monoclonal mouse antibody (EMD Millipore, #MAB377, 1:500) was used to label granule cells of the cerebellum. Anti-TMEM16A rabbit antibody (Abcam, #ab53212, 1:300) and custom-made anti-TMEM16B rabbit antibody(Huang et al., 2012b) (1:300) were used to label TMEM16A and TMEM16B expressing cells in the inferior olive and cerebellum. Anti-KCa1.1 channel rabbit antibody (Alomone labs, #APC-021, 1:100) and Anti-KCa2.3 channel rabbit antibody (Alomone labs, # APC-025, 1:100) were used to label BK channel alpha subunit and SK3 channel, respectively. All primary antibodies were incubated with sections overnight at 4°C followed by secondary antibodies (1:1000, conjugated with Alexa 488 or Alexa 647, Thermo Fisher Scientific) incubation for 2 hours at room temperature. Images were obtained with a Zeiss 780 inverted confocal microscope using a 63x/1.4 NA Oil Plan-Apochromat DIC objective. Representative images from at least three repeats were shown in the figures.

RT-PCR and Western Blotting—For RT-PCR, retina, olfactory bulbs, hippocampi, and medulla oblongata were dissected from TMEM16B knockout mice and wild type controls (1.5 – 2 months old). Total RNA was extracted with Trizol® reagent (Life Technologies) and purified with RNeasy MinElute Kit (Qiagen) following manufacturers' instructions. Two micrograms of each total RNA were reverse transcribed into cDNA using the SuperScript® III First-Strand Synthesis System (Life Technologies). RT-PCR was performed using the Platinum® Pfx DNA Polymerase (Life Technologies) with primers specific to *TMEM16B* and β-actin as described before (Huang et al., 2012b). PCR products were resolved on agarose gels. Amplicon identities were confirmed by sequencing. Representative images from at least two repeats were shown in the figures.

For Western blotting, retina, hippocampi, and medulla oblongata were dissected from TMEM16B knockout and wild type control mice (2–2.5 months old). Tissues were homogenized in lysis buffer containing 1% cholic acid, 1% Triton-X, Complete® Protease Inhibitor Cocktail (Roche), and 0.1 M phosphate-buffered-saline (PBS, pH 7.4) on ice with a Dounce Homogenizer. Homogenates were lysed on ice for 30 minutes, followed by sonication. Lysates were incubated on ice for another 30 minutes, and centrifuged at 16,000g for 40 minutes at 4°C. Supernatants were collected. Protein contents were measured using the Advanced Protein Assay (Cytoskeleton Inc). Protein samples were resolved by SDS-polyacrylamide gel electrophoresis in NuPage 4–12% polyacrylamide Bis-Tris gels (Life Technologies), and transferred to polyvinylidene fluoride (PVDF) membranes. Because the extracellular epitope in TMEM16B protein that is recognized by our rabbit anti-TMEM16B antibody is close to a glycosylation site, detection in the blots was enhanced by treatment with Peptide N-Glycosidase F (PNGase F, Prozyme) at 37°C for 2 hours to de-glycosylate proteins. The blots were subsequently incubated with primary antibodies overnight at 4°C, followed by incubation with HRP-linked secondary antibodies. Signals were visualized using Western Lightening® Plus-ECL reagent (Perkin Elmer) and CL-XPosure Film (Thermo Scientific). The following primary antibodies were used: purified polyclonal rabbit anti-TMEM16B (Huang et al., 2012b) (1:500) and mouse anti-β-tubulin (1:1,000, Covance). Representative images from at least two repeats were shown in the figures.

Acute Brain Stem Slice Preparation—TMEM16B wildtype and knockout mice (postnatal day 10–16) of either sex were anesthetized with isoflurane and decapitated. The brain was rapidly removed and the regions of brain stem containing the inferior olive were dissected. Brain slices of 250 μM coronal sections were cut in ice-cold NMDG aCSF containing (in mM): 92 NMDG, 2.5 KCl, 1.25 NaH_2PO_4, 25 $NaHCO_3$, 20 HEPES, 25 glucose, 2 thiourea, 5 Na-ascorbate, 3 Na-pyruvate, 10 $MgSO_4$, 0.5 $CaCl_2$; then transferred into HEPES holding solution ((in mM) 92 NaCl, 2.5 KCl, 1.25 NaH_2PO_4, 25 $NaHCO_3$, 20 HEPES, 25 glucose, 2 thiourea, 5 Na-ascorbate, 3 Na-pyruvate, 2 $MgSO_4$, 2 $CaCl_2$) for a 12-minutes incubation at 33 °C. The brain slices were stabilized in aCSF (composition given below) and equilibrated with 5% CO_2 + 95% O_2 for 2 hours at room temperature before recording.

Slice Electrophysiology—Brain slices were continuously perfused with aCSF equilibrated with 5% CO_2 + 95% O_2 at 32–33°C for current-clamp recording (or room temperature for voltage-clamp recording to ensure stable, longer-term GΩ-seal). Normal aCSF was composed of (in mM): 124 NaCl, 5 KCl, 2.6 $CaCl_2$, 1.3 $MgCl_2$, 1.25 NaH_2PO_4, 26 $NaHCO_3$, 10 glucose (total 136.8 Cl^-), pH7.4, equilibrated with 5% CO_2 + 95% O_2. For low-Cl^- experiments, we prepared a modified low Cl^- aCSF by replacing 124 mM NaCl with 108.8 mM Na-aspartate and 15.2 mM NaCl (total 28 Cl^-). Perfusion speed was 4 ml/min.

Whole-cell recordings were performed with a MultiClamp700B amplifier interfacing with a Digidata1550A A/D converter. The signals were sampled at 10 kHz and filtered at 4 kHz for currents, or 10 kHz for voltage signals. Data were acquired and analyzed with pCLAMP 10.0 software (Molecular Devices). For current-clamp recording, pipette resistance was 4–6

MΩ when filled with internal solution containing (in mM): 125 K-gluconate, 15 KCl, 10 HEPES, 2 MgATP, 0.3 NaGTP, 10 Na_2phosphocreatine, 0.2 EGTA, pH 7.25. For TMEM16B WT mice, the inferior olive neurons in the principle nuclei were identified by anatomical location and verified by the characteristic firing properties such as the hyperpolarization-induced rebound low-threshold Ca^{2+} spikes and the long afterdepolarization. For the TMEM16B KO mice, mCherry fluorescence was imaged to identify IO neurons. After GΩ-seal establishment and membrane break-through, the membrane rest potential was monitored for 10 min until it is stabilized before recording of currents or action potentials. IO neurons with resting potential more positive than −40 mV were discarded. For voltage-clamp recordings, pipette resistance was 1.5–2.5 MΩ when filled with internal solution containing (in mM): 110 Cs-methanesulphonate, 20 tetraethylammonium chloride (TEACl), 8 KCl, 10 HEPES, 2 MgATP, 0.3 NaGTP, 0.2 EGTA, 5 QX-314-Br, pH 7.25 (total 28 Cl^-); in some experiments (as indicated in the text and legends) internal solution with 5 EGTA were used. The IO neurons were held at −80 mV. Stimulation protocols were as indicated in the text. For pharmacological experiments, 400 μM Cd^{2+} or 100 μM niflumic acid (NFA) was added to extracellular aCSF. ADP duration was defined by action potential duration of 90% repolarization (Figure 4A). AHP duration was measured as the time duration when membrane potential stays below the steady state potential in response to the continuous excitatory stimulus. Slope of AHP was measured as the slope (V/s) from the maximum AHP to the start of next action potential. Data were collected and processed randomly, and were presented as means ± standard errors of the mean. A Student's *t* test was used for comparison of two groups, and a paired Student's *t* test was used for comparisons before and after drug exposure. Values of $p < 0.05$ were considered significant.

QUANTIFICATION AND STATISTICAL ANALYSIS

All statistical analyses were based on two-tailed comparisons and were performed using either Origin (Origin Lab) or GraphPad Prism (GraphPad Software). Sample number (n) values are indicated in the results section and Figure legends. Data are presented as mean ± standard error of the mean (SEM). Although no statistical tests were used to predetermine sample sizes, our sample sizes are consistent with previous publications (Bal and McCormick, 1997; Heiney et al., 2014; Llinas and Yarom, 1981a, b). *p* values less than 0.05 were considered statistically significant. Details on particular quantification procedures and analyses are provided in corresponding section of STAR Methods section.

DATA AND CODE AVAILABILITY

All relevant data and code supporting this study are available from the lead contact upon reasonable request.

Supplementary Material

Refer to Web version on PubMed Central for supplementary material.

Acknowledgments

We thank Dr. Woo-ping Ge for the assistance on electrophysiology. We thank the Crabtree lab (Stanford University) for their help with the targeting of the ES cells. This work was supported by the Whitehead Foundation (H.Y.), NIH-R00NS086916 (H.Y.) and NIH-R01NS069229 (L.Y.J.). L.Y.J. is a Howard Hughes Medical Institute investigator.

References

Adelman JP, Maylie J, Sah P. Small-conductance Ca2+-activated K+ channels: form and function. Annu Rev Physiol. 2012; 74:245–269. [PubMed: 21942705]

Bal T, McCormick DA. Synchronized oscillations in the inferior olive are controlled by the hyperpolarization-activated cation current I(h). J Neurophysiol. 1997; 77:3145–3156. [PubMed: 9212264]

Berkefeld H, Sailer CA, Bildl W, Rohde V, Thumfart JO, Eble S, Klugbauer N, Reisinger E, Bischofberger J, Oliver D, et al. BKCa-Cav channel complexes mediate rapid and localized Ca2+-activated K+ signaling. Science. 2006; 314:615–620. [PubMed: 17068255]

Billig GM, Pal B, Fidzinski P, Jentsch TJ. Ca^{2+}-activated Cl^{-} currents are dispensable for olfaction. Nat Neurosci. 2011; 14:763–769. [PubMed: 21516098]

Bond CT, Maylie J, Adelman JP. SK channels in excitability, pacemaking and synaptic integration. Curr Opin Neurobiol. 2005; 15:305–311. [PubMed: 15922588]

Caputo A, Caci E, Ferrera L, Pedemonte N, Barsanti C, Sondo E, Pfeffer U, Ravazzolo R, Zegarra-Moran O, Galietta LJ. TMEM16A, a membrane protein associated with calcium-dependent chloride channel activity. Science. 2008; 322:590–594. [PubMed: 18772398]

Catterall WA. Voltage-gated calcium channels. Cold Spring Harb Perspect Biol. 2011; 3:a003947. [PubMed: 21746798]

Catterall WA, Perez-Reyes E, Snutch TP, Striessnig J. International Union of Pharmacology. XLVIII. Nomenclature and structure-function relationships of voltage-gated calcium channels. Pharmacol Rev. 2005; 57:411–425. [PubMed: 16382099]

Chen H, Ordog T, Chen J, Young DL, Bardsley MR, Redelman D, Ward SM, Sanders KM. Differential gene expression in functional classes of interstitial cells of Cajal in murine small intestine. Physiol Genomics. 2007; 31:492–509. [PubMed: 17895395]

Cho H, Yang YD, Lee J, Lee B, Kim T, Jang Y, Back SK, Na HS, Harfe BD, Wang F, et al. The calcium-activated chloride channel anoctamin 1 acts as a heat sensor in nociceptive neurons. Nat Neurosci. 2012; 15:1015–1021. [PubMed: 22634729]

Choi S, Yu E, Kim D, Urbano FJ, Makarenko V, Shin HS, Llinas RR. Subthreshold membrane potential oscillations in inferior olive neurons are dynamically regulated by P/Q- and T-type calcium channels: a study in mutant mice. J Physiol. 2010; 588:3031–3043. [PubMed: 20547676]

Coesmans M, Weber JT, De Zeeuw CI, Hansel C. Bidirectional parallel fiber plasticity in the cerebellum under climbing fiber control. Neuron. 2004; 44:691–700. [PubMed: 15541316]

Davis AJ, Forrest AS, Jepps TA, Valencik ML, Wiwchar M, Singer CA, Sones WR, Greenwood IA, Leblanc N. Expression profile and protein translation of TMEM16A in murine smooth muscle. Am J Physiol Cell Physiol. 2010; 299:C948–959. [PubMed: 20686072]

De Gruijl, JR., Bosman, LWJ., De Zeeuw Chris, I., De Jeu, MTG. Inferior Olive: All Ins and Outs. In: Manto, M.Schmahmann, JD.Rossi, F.Gruol, DL., Koibuchi, N., editors. Handbook of the Cerebellum and Cerebellar Disorders. Springer; Netherlands: 2013. p. 1013-1058.

De Zeeuw CI, Simpson JI, Hoogenraad CC, Galjart N, Koekkoek SK, Ruigrok TJ. Microcircuitry and function of the inferior olive. Trends Neurosci. 1998; 21:391–400. [PubMed: 9735947]

Fakler B, Adelman JP. Control of K(Ca) channels by calcium nano/microdomains. Neuron. 2008; 59:873–881. [PubMed: 18817728]

Frings S, Reuter D, Kleene SJ. Neuronal Ca2+-activated Cl- channels--homing in on an elusive channel species. Prog Neurobiol. 2000; 60:247–289. [PubMed: 10658643]

Gomez-Pinilla PJ, Gibbons SJ, Bardsley MR, Lorincz A, Pozo MJ, Pasricha PJ, Van de Rijn M, West RB, Sarr MG, Kendrick ML, et al. Ano1 is a selective marker of interstitial cells of Cajal in the

human and mouse gastrointestinal tract. Am J Physiol Gastrointest Liver Physiol. 2009; 296:G1370–1381. [PubMed: 19372102]

Hartzell C, Putzier I, Arreola J. Calcium-activated chloride channels. Annu Rev Physiol. 2005; 67:719–758. [PubMed: 15709976]

Heiney SA, Wohl MP, Chettih SN, Ruffolo LI, Medina JF. Cerebellar-dependent expression of motor learning during eyeblink conditioning in head-fixed mice. J Neurosci. 2014; 34:14845–14853. [PubMed: 25378152]

Hille, B. Ion channels of excitable membranes. 3. Sunderland, MA: Sinauer; 2001.

Huang F, Rock JR, Harfe BD, Cheng T, Huang X, Jan YN, Jan LY. Studies on expression and function of the TMEM16A calcium-activated chloride channel. Proc Natl Acad Sci U S A. 2009; 106:21413–21418. [PubMed: 19965375]

Huang F, Zhang H, Wu M, Yang H, Kudo M, Peters CJ, Woodruff PG, Solberg OD, Donne ML, Huang X, et al. Calcium-activated chloride channel TMEM16A modulates mucin secretion and airway smooth muscle contraction. Proc Natl Acad Sci U S A. 2012a; 109:16354–16359. [PubMed: 22988107]

Huang WC, Xiao S, Huang F, Harfe BD, Jan YN, Jan LY. Calcium-activated chloride channels (CaCCs) regulate action potential and synaptic response in hippocampal neurons. Neuron. 2012b; 74:179–192. [PubMed: 22500639]

Lancaster B, Nicoll RA. Properties of two calcium-activated hyperpolarizations in rat hippocampal neurones. J Physiol. 1987; 389:187–203. [PubMed: 2445972]

Lang EJ, Apps R, Bengtsson F, Cerminara NL, De Zeeuw CI, Ebner TJ, Heck DH, Jaeger D, Jorntell H, Kawato M, et al. The Roles of the Olivocerebellar Pathway in Motor Learning and Motor Control. A Consensus Paper. Cerebellum. 2017; 16:230–252. [PubMed: 27193702]

Lang EJ, Sugihara I, Llinas R. Differential roles of apamin- and charybdotoxin-sensitive K+ conductances in the generation of inferior olive rhythmicity in vivo. J Neurosci. 1997; 17:2825–2838. [PubMed: 9092604]

Liu B, Linley JE, Du X, Zhang X, Ooi L, Zhang H, Gamper N. The acute nociceptive signals induced by bradykinin in rat sensory neurons are mediated by inhibition of M-type K+ channels and activation of Ca2+-activated Cl- channels. J Clin Invest. 2010; 120:1240–1252. [PubMed: 20335661]

Liu P, Jenkins NA, Copeland NG. A highly efficient recombineering-based method for generating conditional knockout mutations. Genome Res. 2003; 13:476–484. [PubMed: 12618378]

Llinas R, Yarom Y. Electrophysiology of mammalian inferior olivary neurones in vitro. Different types of voltage-dependent ionic conductances. J Physiol. 1981a; 315:549–567. [PubMed: 6273544]

Llinas R, Yarom Y. Properties and distribution of ionic conductances generating electroresponsiveness of mammalian inferior olivary neurones in vitro. J Physiol. 1981b; 315:569–584. [PubMed: 7310722]

Llinas RR. The olivo-cerebellar system: a key to understanding the functional significance of intrinsic oscillatory brain properties. Front Neural Circuits. 2013; 7:96. [PubMed: 24478634]

Mathy A, Ho SS, Davie JT, Duguid IC, Clark BA, Hausser M. Encoding of oscillations by axonal bursts in inferior olive neurons. Neuron. 2009; 62:388–399. [PubMed: 19447094]

Mercer AJ, Rabl K, Riccardi GE, Brecha NC, Stella SL Jr, Thoreson WB. Location of release sites and calcium-activated chloride channels relative to calcium channels at the photoreceptor ribbon synapse. J Neurophysiol. 2011; 105:321–335. [PubMed: 21084687]

Najafi F, Medina JF. Beyond “all-or-nothing” climbing fibers: graded representation of teaching signals in Purkinje cells. Front Neural Circuits. 2013; 7:115. [PubMed: 23847473]

Neher E. Vesicle pools and Ca2+ microdomains: new tools for understanding their roles in neurotransmitter release. Neuron. 1998; 20:389–399. [PubMed: 9539117]

Pedemonte N, Galietta LJ. Structure and function of TMEM16 proteins (anoctamins). Physiol Rev. 2014; 94:419–459. [PubMed: 24692353]

Pifferi S, Dibattista M, Menini A. TMEM16B induces chloride currents activated by calcium in mammalian cells. Pflugers Arch. 2009; 458:1023–1038. [PubMed: 19475416]

Rasmussen A, Jirenhed DA, Zucca R, Johansson F, Svensson P, Hesslow G. Number of spikes in climbing fibers determines the direction of cerebellar learning. J Neurosci. 2013; 33:13436–13440. [PubMed: 23946401]

Sah P, Faber ES. Channels underlying neuronal calcium-activated potassium currents. Prog Neurobiol. 2002; 66:345–353. [PubMed: 12015199]

Sailer CA, Kaufmann WA, Marksteiner J, Knaus HG. Comparative immunohistochemical distribution of three small-conductance Ca2+-activated potassium channel subunits, SK1, SK2, and SK3 in mouse brain. Mol Cell Neurosci. 2004; 26:458–469. [PubMed: 15234350]

Salkoff L, Butler A, Ferreira G, Santi C, Wei A. High-conductance potassium channels of the SLO family. Nat Rev Neurosci. 2006; 7:921–931. [PubMed: 17115074]

Schroeder BC, Cheng T, Jan YN, Jan LY. Expression cloning of TMEM16A as a calcium-activated chloride channel subunit. Cell. 2008; 134:1019–1029. [PubMed: 18805094]

Schweighofer N, Doya K, Kawato M. Electrophysiological properties of inferior olive neurons: A compartmental model. J Neurophysiol. 1999; 82:804–817. [PubMed: 10444678]

Scudieri P, Caci E, Bruno S, Ferrera L, Schiavon M, Sondo E, Tomati V, Gianotti A, Zegarra-Moran O, Pedemonte N, et al. Association of TMEM16A chloride channel overexpression with airway goblet cell metaplasia. J Physiol. 2012; 590:6141–6155. [PubMed: 22988141]

Stocker M. Ca(2+)-activated K+ channels: molecular determinants and function of the SK family. Nat Rev Neurosci. 2004; 5:758–770. [PubMed: 15378036]

Stohr H, Heisig JB, Benz PM, Schoberl S, Milenkovic VM, Strauss O, Aartsen WM, Wijnholds J, Weber BH, Schulz HL. TMEM16B, a novel protein with calcium-dependent chloride channel activity, associates with a presynaptic protein complex in photoreceptor terminals. J Neurosci. 2009; 29:6809–6818. [PubMed: 19474308]

Storm JF. Action potential repolarization and a fast after-hyperpolarization in rat hippocampal pyramidal cells. J Physiol. 1987; 385:733–759. [PubMed: 2443676]

Yang C, Delay RJ. Calcium-activated chloride current amplifies the response to urine in mouse vomeronasal sensory neurons. J Gen Physiol. 2010; 135:3–13. [PubMed: 20038523]

Yang Y, Lisberger SG. Purkinje-cell plasticity and cerebellar motor learning are graded by complex-spike duration. Nature. 2014; 510:529–532. [PubMed: 24814344]

Yang YD, Cho H, Koo JY, Tak MH, Cho Y, Shim WS, Park SP, Lee J, Lee B, Kim BM, et al. TMEM16A confers receptor-activated calcium-dependent chloride conductance. Nature. 2008; 455:1210–1215. [PubMed: 18724360]

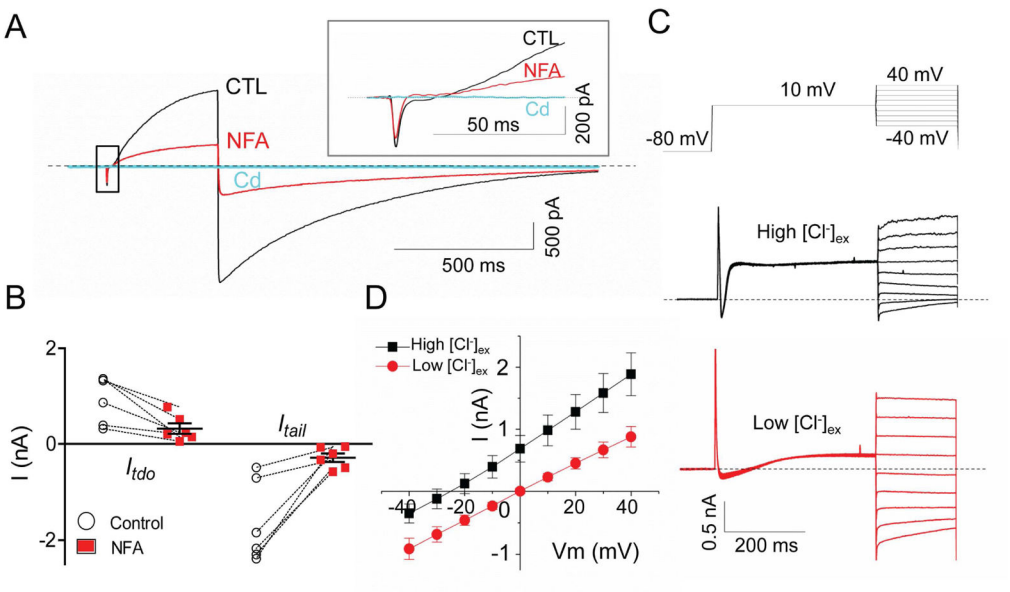

Figure 1. A large Ca^{2+}-activated Cl^- current exists in inferior olivary (IO) neurons

(A) Depolarizing an IO neuron to +10 mV elicited a large Ca^{2+} sensitive, time-dependent, outward rectifying current (I_{tdo}) with a slow decaying tail current (I_{tail}) at the end of depolarization. This Ca^{2+}-sensitive current (CTL) can be inhibited by 100 μM niflumic acid (NFA) and it is completely abolished by 400 μM Cd^{2+}, a potent voltage-gated Ca^{2+} channel blocker.

(B) Summary of NFA inhibitory effects on I_{tdo} and I_{tail} (paired *t*-test: $n = 6$. $p = 0.014$ for I_{tdo} and $p = 0.005$ for I_{tail}). Error bar represents SEM.

(C) Measurements of reversal potential in different extracellular Cl^- concentrations indicate that the Ca^{2+}-sensitive current in IO neurons arises from Ca^{2+}-activated Cl^- channels (CaCCs). The voltage protocol is shown at the top.

(D) The *I–V* relation in the presence of high and low extracellular Cl^- ($[Cl^-]_{ex}$) concentrations. $n = 11$ and 6 for high (136.8 mM) and low (28 mM) $[Cl^-]_{ex}$ concentrations, respectively. Error bar represents SEM.

Dotted lines mark $I = 0$.

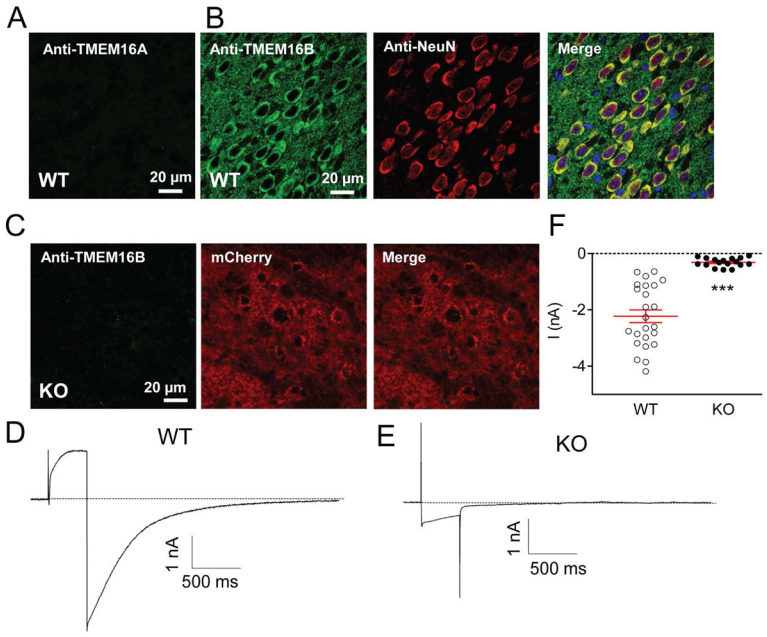

Figure 2. TMEM16B but not TMEM16A is highly expressed in IO neurons

(A) TMEM16A is not expressed in IO neurons.

(B) TMEM16B is expressed in IO neurons, which express neuronal marker NeuN.

(C) TMEM16B expression is eliminated and farnesylated mCherry expression is introduced in the IO neurons from TMEM16B knockout (KO) mice.

(D) Depolarization to +10 mV induced large Ca^{2+}-sensitive I_{tdo} and I_{tail} in WT IO neurons.

(E) Genetic ablation of TMEM16B completely eliminated I_{tdo} and I_{tail} in TMEM16B KO IO neurons, indicating that TMEM16B CaCC mediates the Ca^{2+}-sensitive I_{tdo} and I_{tail} in IO neurons. The small inward current was carried by the high-threshold voltage-gated Ca^{2+} channels in IO neurons.

(F) Comparison of I_{tail} amplitudes of the IO neurons from TMEM16B WT and KO mice. To avoid membrane capacitive currents, tail current amplitudes 50 ms after the repolarization (−80 mV) were measured. Unpaired *t*-test: $n = 24$ for WT and $n = 17$ for TMEM16B KO mice, *** $p = 1.3 \times 10^{-8}$. Error bar represents SEM. Dotted lines mark $I = 0$.

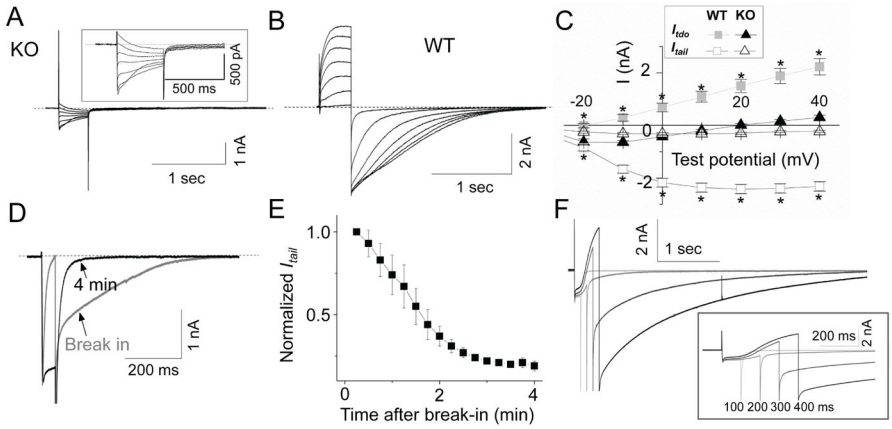

Figure 3. TMEM16B-CaCC can be activated by dendritic high-threshold voltage gated Ca^{2+} (Ca_V) channels

(A, B) Current traces elicited from TMEM16B knockout (KO, A) and wildtype (WT, B) IO neurons. Membrane potential was depolarized from −20 to +40 mV to open the dendritic high-threshold Ca_V channels and then repolarized to −80 mV.

(c) The *I-V* relationship of peak I_{tdo} and I_{tail} current from WT and KO IO neurons. Peak current amplitudes were measured at the end of the depolarization pulses and tail current amplitudes were measured at 50 ms after the repolarization pulse. Unpaired *t*-test: $n = 24$ for WT and $n = 17$ for KO. * $p = 0.0006$ for I_{tdo} and $p = 2.7 \times 10^{-8}$ for I_{tail}. Error bars represent SEM.

(D) Current changes in response to a 50 ms depolarization to 0 mV right after membrane break-in to establish whole-cell patch clamp (grey) and 4 minutes later (black), after allowing 5 mM EGTA to diffuse into the WT IO neuron.

(E) Time course of the tail current while 5 mM EGTA diffuses into the cell, leading to total elimination of the CaCC-mediated CaCC tail current. The tail currents were measured 50 ms after the repolarization pulse and normalized to the amplitudes of the initial tail current. $n = 4$. Error bars represent SEM.

(F) Prolongation of depolarization enabled opening of TMEM16B-CaCC, resulting in a gradual increase of the outward I_{tdo} and I_{tail} current in the presence of 5 mM EGTA. Current was recorded after EGTA had entered the cell under whole-cell patch recording. Inset, enlarged view of currents at the beginning of the test pulses.

Dotted lines mark $I = 0$.

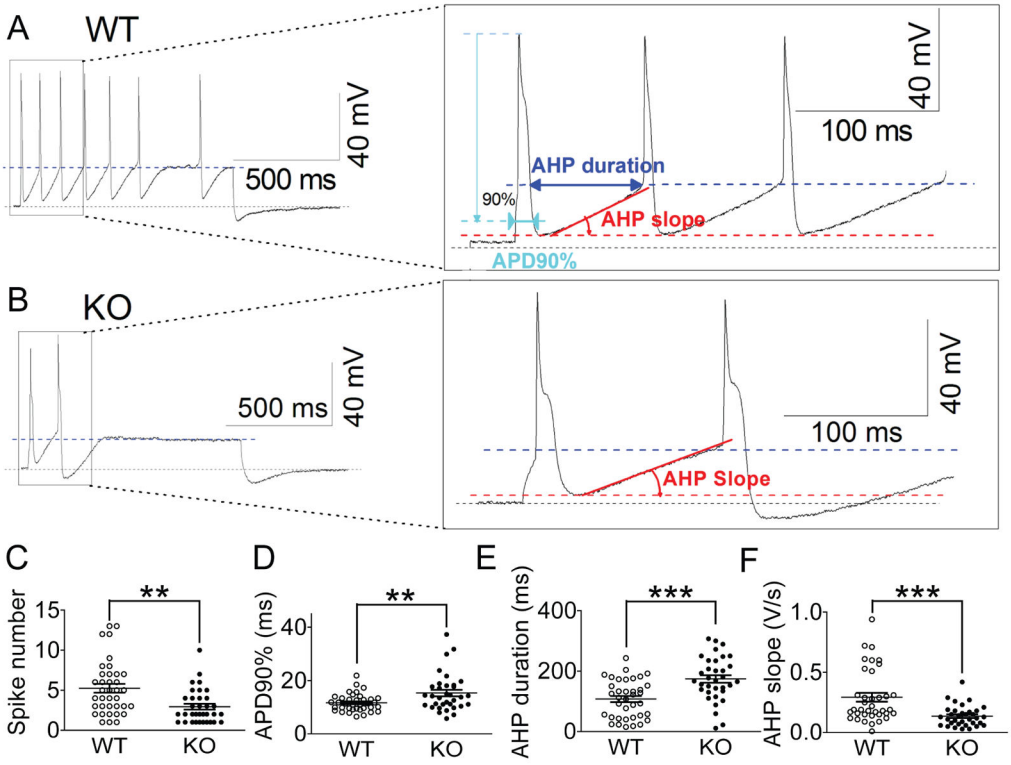

Figure 4. IO neurons from TMEM16B KO mice exhibited reduced membrane excitability

(A, B) Representative firing of IO neurons from wildtype (WT, A) and TMEM16B knockout (KO, B) mice in response to a 400 pA excitatory stimulus for 1 second. Insets show expanded view of the spikes. The black, red and blue dotted lines mark the resting potential, the maximum repolarization potential, and the steady state potential in response to continuous 400 pA excitatory stimulus, respectively. Definitions of spike parameters are labeled with blue, cyan and red color.

(C) The average number of spikes for WT and TMEM16B KO IO neurons in response to the excitatory stimulus. $p = 0.001$. Error bar represents SEM.

(D) The averaged action potential duration of 90% repolarization (APD90%) of the first high-threshold Ca^{2+} spike from WT and TMEM16B KO IO neurons. APD90% was used to define after depolarization. $p = 0.004$. Error bar represents SEM.

(E) The averaged after-hyperpolarization (AHP) duration of WT and TMEM16B KO IO neurons. $p = 0.0001$. Error bar represents SEM.

(F) The averaged AHP slope of WT and TMEM16B KO IO neurons. $p = 0.0002$. Error bar represents SEM.

Unpaired *t*-test: 37 IO neurons from 12 TMEM16B WT mice and 34 IO neuron from 10 TMEM16B KO mice, ** $p < 0.01$, *** $p < 0.001$.

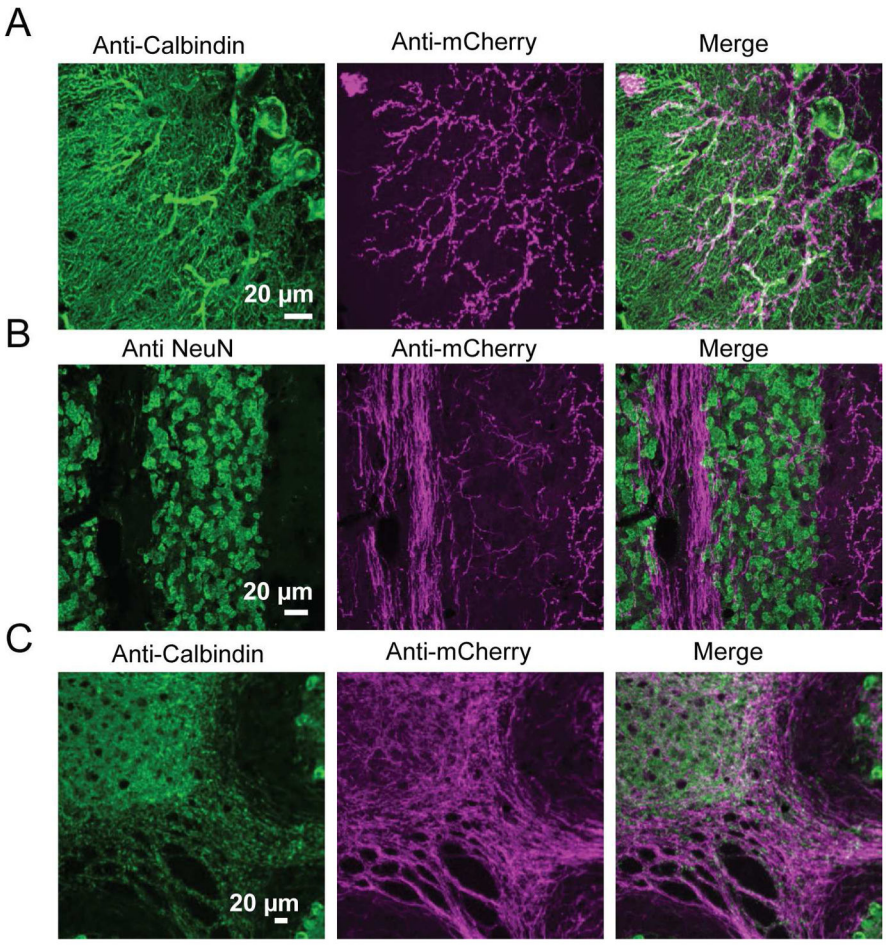

Figure 5. TMEM16B-CaCC is specifically expressed in inferior olivary neurons in the olivo-cerebellar system

(A) No TMEM16B expression was observed in the Purkinjie cell (PC) layer. Anti-calbindin labels PCs. The farnesylated mCherry signal from TMEM16B KO mice was used to label TMEM16B expressing cells. mCherry was only detected in climbing fibers from IO neurons.

(B) No TMEM16B expression was observed in the granule cell (GC) layer. Anti-NeuN labels GCs. mCherry was only detected in climbing fibers.

(C) No TMEM16B expression was observed in the deep cerebellar nucleus (DCN). Anti-calbindin labels DCN neurons. mCherry was only detected in climbing fibers.

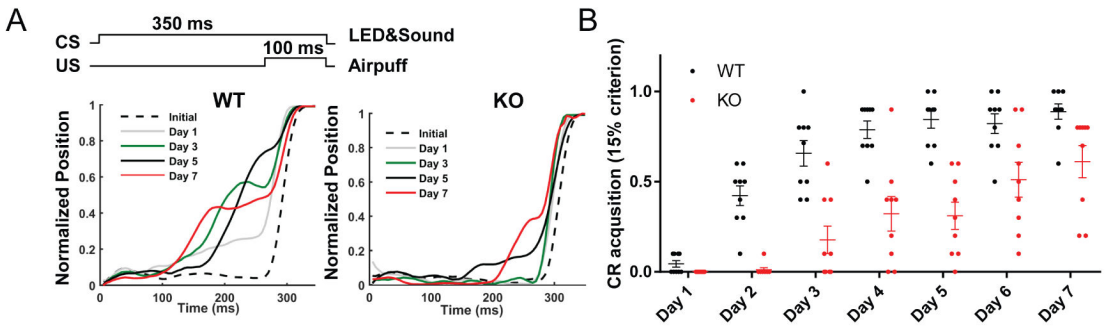

Figure 6. TMEM16B knockout (KO) mice exhibited impaired motor learning assessed via eyeblink classical conditioning

(A) Acquisition of conditioned responses (CR) of a wildtype (WT) and a TMEM16B KO mouse during a seven-day training section. The eyeblink conditioning training paradigm is shown on top, with the conditioned stimulus (CS, 350 ms, 2.7 Hz tone and white light LED) and the 100 ms unconditioned stimulus (US, airpuff, 4~5psi) starting at 250 ms after the initiation of CS. CS and US are co-terminated. Each animal was trained for 90 paired CS-US trials followed by 10 CS-only trials in seven consecutive days. The eyelid closure traces during the last 10 CS-US trials were averaged and shown in the figure. The initial responses shown in the dashed lines refer to the average of the first 10 CS-US trials for the naïve mice on Day 1.

(B) TMEM16B KO exhibited impaired CR acquisition. CR acquisition was defined by eyelid closures that are greater than 15% of complete eye closure during the last 10 CS-only trials at the end of each training day. A repeated measure ANOVA was used for comparison of CR acquisition for TMEM16B KO and WT mice in all the training sessions. There were highly significant differences of the factors genotype ($F(1,16) = 56.93$, $p < 0.0001$) and time ($F(6,96) = 40.63$, $p < 0.0001$). The interaction was also significant ($F(6,96) = 4.215$, $p = 0.0008$).